Tailoring the Void Size of Iron Oxide@Carbon Yolk–Shell Structure for Optimized Lithium Storage

Hongwei Zhang, Liang Zhou, Owen Noonan, Darren J. Martin, Andrew K. Whittaker, and Chengzhong Yu**

High-capacity lithium-ion battery anode materials, such as transition metal oxides, Sn and Si, suffer from large volume expansion during lithiation, which causes capacity decay. Introducing sufficient void space to accommodate the volume change is essential to achieve prolonged cycling stability. However, excessive void space may significantly compromise the volumetric energy density. Herein, a method to control the void size in iron oxide@carbon (FeO_x@C) yolk–shell structures is developed and the relationship between the void space and electrochemical performance is demonstrated. With an optimized void size, the FeO_x@C yolk–shell structure exhibits the best cycling performance. A high reversible capacity of ≈810 mA h g^{-1} is obtained at 0.2 C, maintaining 790 mA h g^{-1} after 100 cycles. This contrasts with FeO_x@C materials having either smaller or larger void sizes, in which significant capacity fading is observed during cycling. This contribution provides an effective approach to alleviate the volume expansion problem, which can be generally applied to other anode materials to improve their performance in LIBs.

1. Introduction

Stimulated by the widespread usage of portable electronics and the rapid growth of electric vehicles, energy storage is expected to play an increasingly important role in our daily life.[1] Among the myriad energy storage technologies, lithium ion batteries (LIBs) are particularly attractive due to their relatively high energy density.[2] Although LIBs outperform other competing technologies in terms of energy density, the energy that current LIBs can deliver is not sufficient to fully meet the demands of emerging applications, such as electric vehicles. Since energy density is the product of capacity and operating voltage, it can be improved by employing either high-capacity electrodes or high-voltage cathode materials. Graphite, although ubiquitously used as the anode material in current designs, is limited by a theoretical capacity of 372 mA h g^{-1}. Therefore, there is extensive interest in the pursuit of high-capacity anode materials.

H. W. Zhang, Dr. L. Zhou, O. Noonan, Prof. D. J. Martin, Prof. A. K. Whittaker, Prof. C. Z. Yu
Australian Institute for Bioengineering and Nanotechnology
The University of Queensland
Brisbane, QLD 4072, Australia
E-mail: l.zhou1@uq.edu.au; c.yu@uq.edu.au

DOI: 10.1002/adfm.201400178

Since the pioneering work by Poizot et al., transition metal oxides (TMOs), such as iron oxides, have attracted much attention as high-capacity anode materials for LIBs.[3,4] However, the practical application of TMOs in LIBs has thus far been hindered by the large volume expansion during lithiation,[5] the formation of thick and unstable solid electrolyte interface (SEI) film,[6,7] and low electrical conductivity,[5,6] which lead to rapid capacity decay during cycling and poor rate performance. To address these issues, several strategies have been developed. The first approach, so-called nanostructuring, relies on the creation of short diffusion paths for lithium ion transport and free space to accommodate the large volume change.[8–14] Although the problems associated with the large volume change can be alleviated in this way, the limited structural stability of the nanostructured TMOs remains problematic. Without protection, bare TMO nanostructures cannot maintain their original morphology due to the pulverization resulting from the repeated lithiation/delithiation.[9] The second approach, known as nanocompositing, aims to improve the structural stability through employing a second component such as carbon as the protective coating layer or matrix. The second component serves three main purposes: 1) to wire the active TMOs, 2) to buffer the volume variation and prevent the aggregation of pulverized active material, and 3) to protect the TMOs against direct contact with the electrolyte which may result in the formation of an unstable SEI film.[6,15–20] However, because this design does not provide appropriate space to accommodate the large volume expansion, the carbon layer may fracture upon lithiation (**Figure 1**a), leading to electrical disconnection, re-exposure of the active materials to electrolyte, and active material aggregation.

Recently, the combination of nanostructuring and nanocompositing strategies has attracted much attention. In this respect, Lou and co-workers rationally designed a coaxial SnO_2@carbon hollow sphere architecture, where the SnO_2 acts as the active core and carbon acts as the conductive shell.[21] This core-shell concept has been extended to Fe_2O_3@polyaniline hollow spheres by Jeong et al.[22] Besides core-shell structured hollow spheres, yolk–shell structures[23] and encapsulation structures[24] have also been reported. The active materials are not limited to TMOs, but also include Si,[25–27] Sn[28,29]

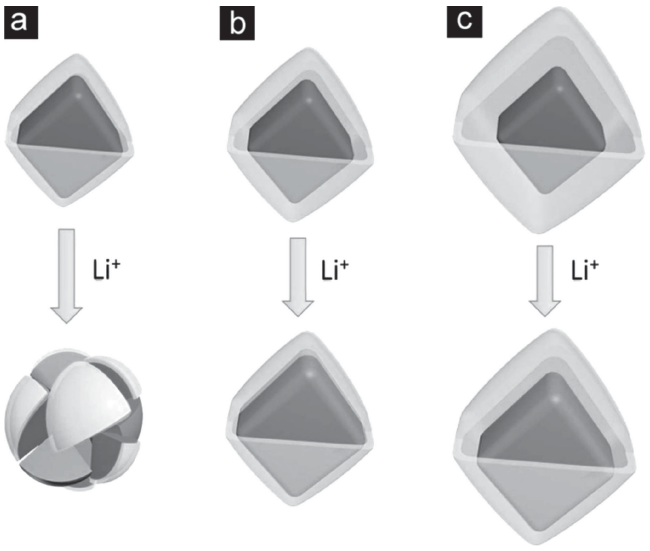

Figure 1. Schematic illustration of FeO_x@C yolk–shell structures with a) small void size, b) optimized void size, and c) excess void size upon lithiation.

and S.[30,31] The key to the success of these novel architectures in improving electrochemical performance lies in their well-defined void space, which allows the active materials to expand freely without breaking the outer protective shell. However, excess void space may significantly compromise the volumetric energy density (Figure 1c).[8] This means the void space acts as a double-edged sword: on one hand, it accommodates the volume expansion, while on the other hand, it sacrifices the volumetric energy density. Thus, it is highly desirable to optimize the void space to achieve high cycling performance while maintaining a reasonable volumetric energy density. However, to the best of our knowledge, there has been very limited success in tuning the void space of high-capacity anode materials with delicate core–shell/yolk–shell/encapsulation structures.[25]

Herein, a novel iron oxide@carbon (FeO_x@C) yolk–shell structure is designed and the void size of the yolk–shell structure is finely tuned to accommodate the volume expansion of the FeO_x core. With an optimized void space, the FeO_x core can expand/contract freely upon lithiation/de-lithiation without breaking the carbon shell (Figure 1b). Thus, excellent cycling performance can be achieved with a minimal sacrifice of volumetric energy density.

2. Results and Discussion

The FeO_x@C yolk–shell structures were experimentally realized as shown schematically in **Figure 2**a. First, well-dispersed α-Fe_2O_3 nanocrystals were prepared by the hydrothermal method using L-arginine as the hydrolysis-controlling agent (Figure 2b and Supporting Information, Figure S1). The α-Fe_2O_3 nanocrystals were then coated with a conformal silica layer through controlled hydrolysis and condensation of TEOS in an alkaline alcohol/water solution, resulting in the formation of α-Fe_2O_3@SiO_2 core-shell nanoparticles (Figure 2c). This was followed by poly-dopamine coating in Tris-buffer and carbonization in Ar, resulting in FeO_x@SiO_2@C nanoparticles (Figure 2d). After removal of the sacrificial silica layer by 2 M NaOH solution, FeO_x@C yolk–shell structures were obtained (Figure 2e). By tuning the amount of TEOS in the silica coating step (Step I), the thickness of the sacrificial silica layer could be adjusted, thus providing control over the void size of the FeO_x@C yolk–shell structures. The samples templated from α-Fe_2O_3@SiO_2 with silica thicknesses of 9, 25, and 45 nm are designated as FeO_x@C-1, FeO_x@C-2, and FeO_x@C-3, respectively.

The α-Fe_2O_3 nanocrystals utilized in this study have an average diameter of ≈170 nm. Considering the volume

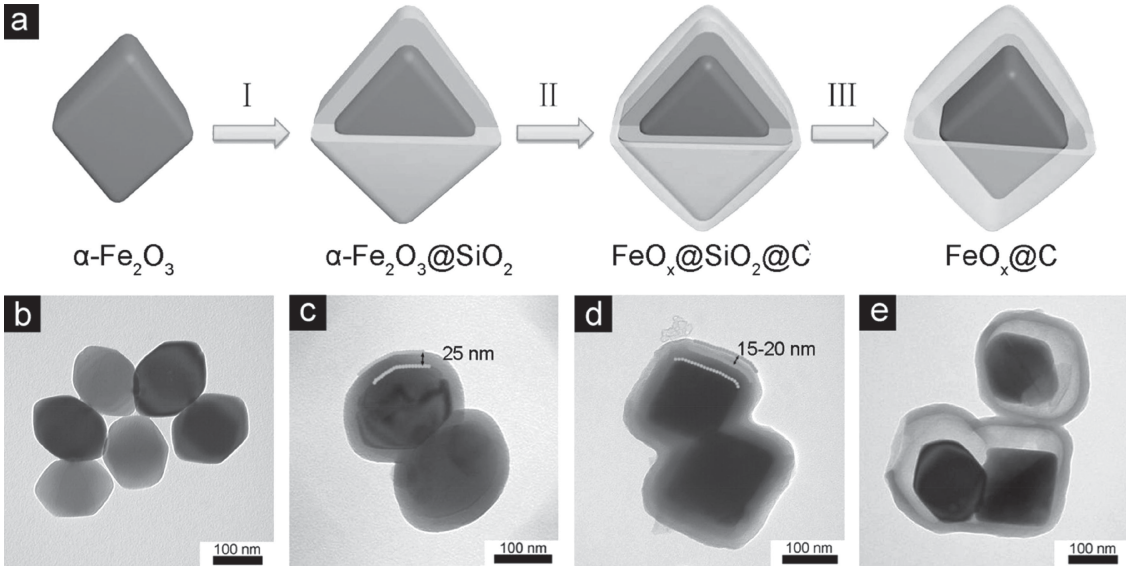

Figure 2. a) Schematic illustration of the synthesis of FeO_x@C yolk–shell structures. Step I: silica coating; step II, poly-dopamine coating and carbonization; step III, silica removal. b) TEM images of bare α-Fe_2O_3 nanoparticle, c) α-Fe_2O_3@SiO_2 core-shell particles with a silica layer of 25 nm, d) FeO_x@SiO_2@C core-shell particles, and e) FeO_x@C-2 yolk–shell particles.

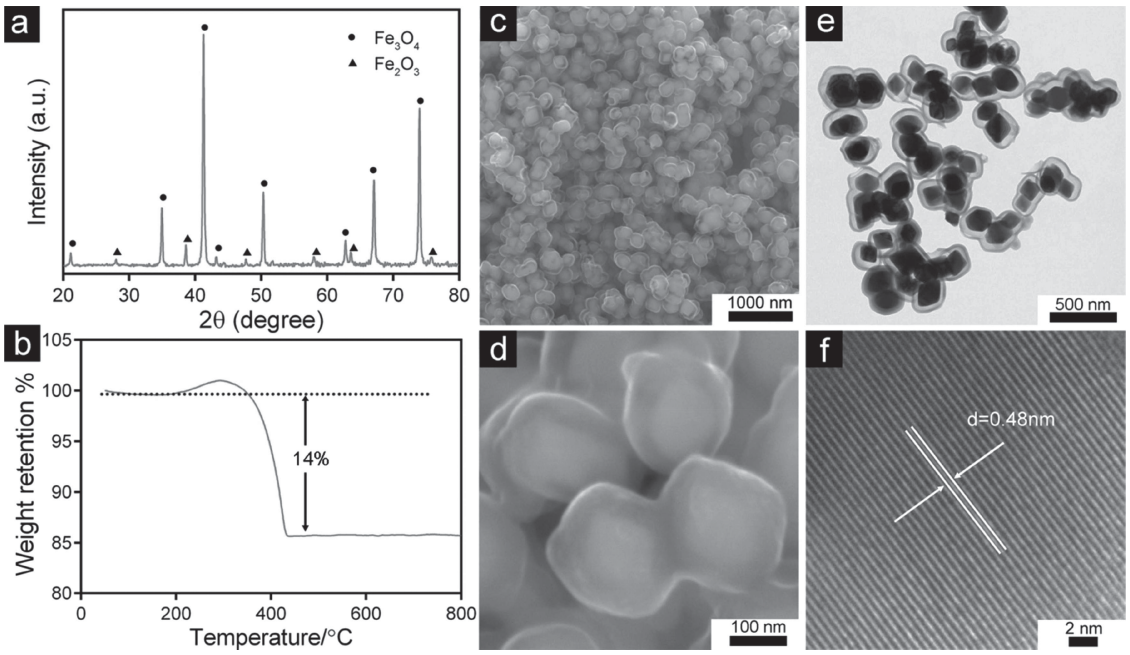

Figure 3. a) XRD pattern, b) TGA thermogram, c,d) SEM, e) TEM, and f) HRTEM images of FeO_x@C-2.

expansion ratio of iron oxide during lithiation (≈0.96), the desirable sacrificial coating layer should have a thickness of 22 nm to allow the FeO_x core to expand freely. Bearing this in mind, the FeO_x@C-2, which is templated from α-Fe_2O_3@SiO_2 with a silica thickness of 25 nm, should be the best candidate and will be discussed in more detail later.

The crystalline structure of the FeO_x@C-2 was investigated by X-ray diffraction (XRD) (**Figure 3**a). The majority of the diffraction peaks, especially for those with high intensity, can be assigned to Fe_3O_4 (magnetite, JCPDS No. 19–0629), while some weak diffraction peaks from α-Fe_2O_3 (hematite, JCPDS No. 33–0664) can also be observed. No diffraction peaks from graphitic carbon can be detected, indicating the amorphous nature of the carbon shell. It has been demonstrated that Fe species can catalyze the graphitization of carbon at temperatures as low as 700 °C.[32] However, due to the "sealing effect" of the silica layer, the iron oxide core and carbon shell is well separated, and the graphitization does not occur during the carbonization step. The effect of calcination temperature on the crystalline phase of FeO_x was also studied. With the increase of calcination temperature from 500 °C to 800 °C, the diffraction peaks for α-Fe_2O_3 weakens gradually (Figure 3a and Supporting Information, Figure S2). However, even at a high calcination temperature of 800 °C, weak diffraction peaks for α-Fe_2O_3 can still be observed. Considering this fact, we just focus on the sample prepared at an intermediate calcination temperature of 700 °C for further structural and electrochemical characterizations.

Thermo gravimetric analysis (TGA) analysis was carried out to determine the carbon content of FeO_x@C-2 (Figure 3b). The slight weight loss below 200 °C is due to the loss of residual moisture. The slight weight gain between 200 °C to 300 °C can be ascribed to the oxidation of Fe_3O_4 to Fe_2O_3. The major weight loss between 300 °C and 430 °C can be attributed to the combustion of carbon in air. The total weight loss of FeO_x@C-2 is 14.0%. Assuming the core material is pure Fe_3O_4, the carbon content of FeO_x@C-2 is estimated to be 16.9% by weight.

The morphology of FeO_x@C-2 was characterized by scanning electron microscopy (SEM) and transmission electron microscopy (TEM). Generally, the FeO_x@C-2 inherits the polyhedron morphology of the α-Fe_2O_3 core (Figure 3c). Due to the thin thickness of the carbon shell, the electron beam can easily penetrate, revealing the inner voids and FeO_x core (Figure 3d). Almost no bare FeO_x particles can be observed in SEM, and only trace amount of Fe can be detected from the X-ray photoelectron spectroscopy (XPS) spectrum (Supporting Information, Figure S3), demonstrating the high quality of the yolk–shell structure. The yolk–shell structure was further confirmed by TEM. As shown in Figure 2e, each FeO_x nanocrystal is encapsulated by a self-supporting carbon shell with a uniform thickness of 15–20 nm. The FeO_x core is closely attached to one side of the carbon shell, leaving a 40–45 nm void space on the other side. The direct facet-to-facet contact of the FeO_x core with the electrically and lithium ion conductive carbon shell makes the core more accessible to both charge carriers. Due to the slight aggregation of α-Fe_2O_3 nanocrystals, carbon shells encapsulating more than one FeO_x nanocrystal can be occasionally observed (Figure 3e). The complete encapsulation ensures even fused FeO_x cores remain protected from further aggregation and direct electrolyte contact. From the high resolution TEM (HRTEM) image (Figure 3f), well-resolved lattice fringes with a spacing of 0.48 nm, which corresponds to the {111} interplane spacing of Fe_3O_4, can be clearly distinguished.

To investigate the role of void size on electrochemical performance, FeO_x@C yolk–shell structures with different void sizes were prepared by tuning the thickness of the sacrificial silica layer from 9 to 45 nm. Templated from α-Fe_2O_3@SiO_2 with a silica layer of 9 (Supporting Information, Figure S4a) and 45 nm (Supporting Information, Figure S4d), FeO_x@C-1

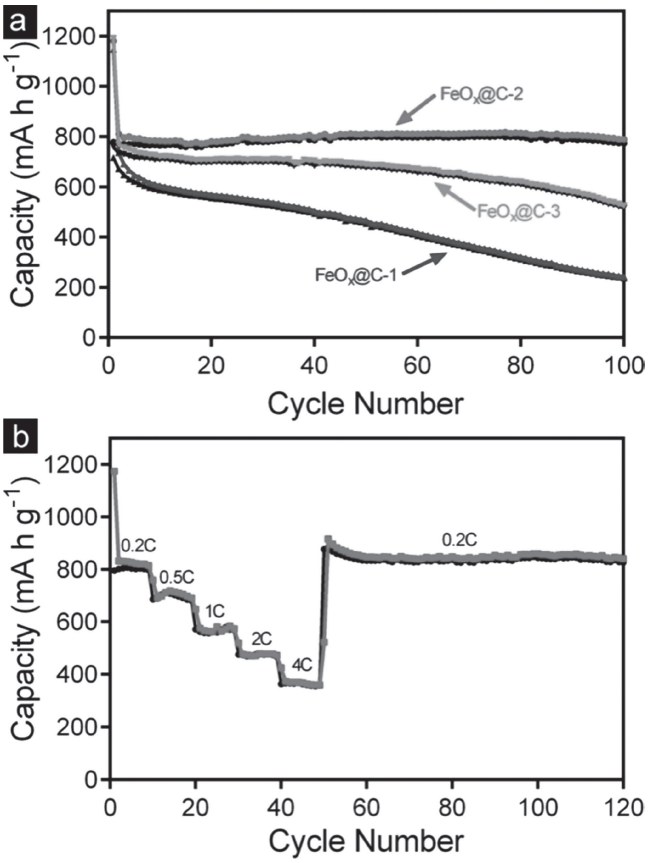

Figure 4. a) Cycling performance of FeO_x@C yolk–shell structures at 0.2 C and b) rate performance of FeO_x@C-2.

and FeO_x@C-3 can be obtained, respectively. SEM and TEM characterization reveal that both FeO_x@C-1 (Supporting Information, Figure S4b,c) and FeO_x@C-3 (Supporting Information, Figure S4e,f) have a yolk–shell structure similar to that of FeO_x@C-2, except for the smaller/larger void size. By carefully observing Figure 2e, S4c and S4f, an interesting phenomenon can be noticed, that is, the larger the void space, the smaller the contact area between FeO_x core and carbon shell. XRD characterization reveals that both FeO_x@C-1 and FeO_x@C-3 have a similar diffraction pattern to that of FeO_x@C-2 (Supporting Information, Figure S5). From the TGA results (Supporting Information, Figure S6a,b), the carbon contents of FeO_x@C-1 and FeO_x@C-3 are estimated to be 16.8% and 16.9% by weight, respectively.

The electrochemical performance of all FeO_x@C yolk–shell structures was then evaluated by a standard method based on an active material/Li half cell configuration. Figure S7a (Supporting Information) shows the cyclic voltammogram (CV) curves of FeO_x@C-2. The peak at 0.48 V from the first cathodic scanning can be ascribed to the conversion of iron oxide to Fe^0 and the formation of solid electrolyte interphase (SEI) layer on the surface of electrode. Meanwhile, a broad peak centred at 2.0 V in the following anodic process is corresponding to the reverse oxidation of Fe^0 to iron oxide. These results are in agreement with the previous reports involving iron oxide-based anode materials.[15,33] In the subsequent cathodic and anodic processes, all peaks overlap well, suggesting a good electrochemical reproducibility of FeO_x@C-2 as an anode material.

Representative galvanostatic charge-discharge profiles of FeO_x@C-2 at a current density of 0.2 C (1 C = 1000 mA g^{-1}) are shown in Figure S7b (Supporting Information). The first lithiation process delivers an initial discharge capacity of 1181 mA h g^{-1} (based on the total mass of FeO_x@C-2), and the subsequent de-lithiation delivers a charge capacity of 778 mA h g^{-1}, resulting in a Coulombic efficiency of 65.9%. The irreversible capacity loss (34.1%) observed in the first cycle is probably associated with the irreversible decomposition of electrolyte and subsequent formation of a solid electrolyte interface (SEI) layer on the surface of the electrode material. A prelithiation strategy can be used to improve the low Coulombic efficiency in practical application.[34] The Coulombic efficiency increases dramatically to 95.3% in the second cycle and levels off at 98–100% in subsequent cycles (Supporting Information, Figure S8). The cycling performances of FeO_x@C yolk–shell structures are shown in **Figure 4**a. It is evident that FeO_x@C-2 outperforms the other two samples in cycling stability. It exhibits almost completely stable cycling performance from the second cycle onwards. Even after 100 cycles, a high capacity of 790 mA h g^{-1} can be maintained, which is 97.4% of the capacity at the second cycle. In sharp contrast, FeO_x@C-1 shows a much inferior cycling performance. Although it delivers a high initial discharge capacity (1148 mA h g^{-1}), the capacity decreases continuously in subsequent cycles; after 100 cycles, a low capacity of 243 mA h g^{-1} is obtained. The cycling stability for FeO_x@C-3 is somewhat better than that of FeO_x@C-1, but still inferior to that of FeO_x@C-2. It delivers an initial discharge capacity of 1191 mA h g^{-1}, maintaining 524 mA h g^{-1} after 100 cycles. The cycling performance of FeO_x@C core-shell structure without any void space was also studied (Supporting Information, Figure S9). The initial discharge capacity is 1133 mA h g^{-1}, and the capacity fades to 184 mA h g^{-1} after 100 cycles. Considering that all samples have almost the same carbon content, the difference in capacity contributed from the carbon shells should be negligible. Thus, the difference in cycling performance should come from the structure (void size) rather than the carbon shells.

The rate performance of FeO_x@C-2 was further investigated by cycling at various current densities ranging from 0.2–4 C (Figure 4b). FeO_x@C-2 delivers a high capacity of 820 mA h g^{-1} at 0.2 C. As the current density increases, the capacity decreases slightly. Even at a high current density of 4 C, the capacity is comparable to the theoretical capacity of graphite. Remarkably, a stable capacity of 840 mA h g^{-1} can be attained when the current is reduced to 0.2 C. The electrochemical performance of FeO_x@C-2 in terms of cycling stability and rate capability is comparable or even superior to those of state-of-the-art iron oxide based anodes in previous reports,[13,15,17,33,35] suggesting the effectiveness of our strategy in addressing the volume expansion issue.

To understand the differences in electrochemical behavior of the three materials, the samples after 100 discharge-charge cycles (in their lithiated state) were investigated by SEM and TEM (**Figure 5**). For FeO_x@C-1 with a small void space, the carbon shells are found to be ruptured (indicated by black arrows in Figure 5b) and almost no intact yolk–shell structures

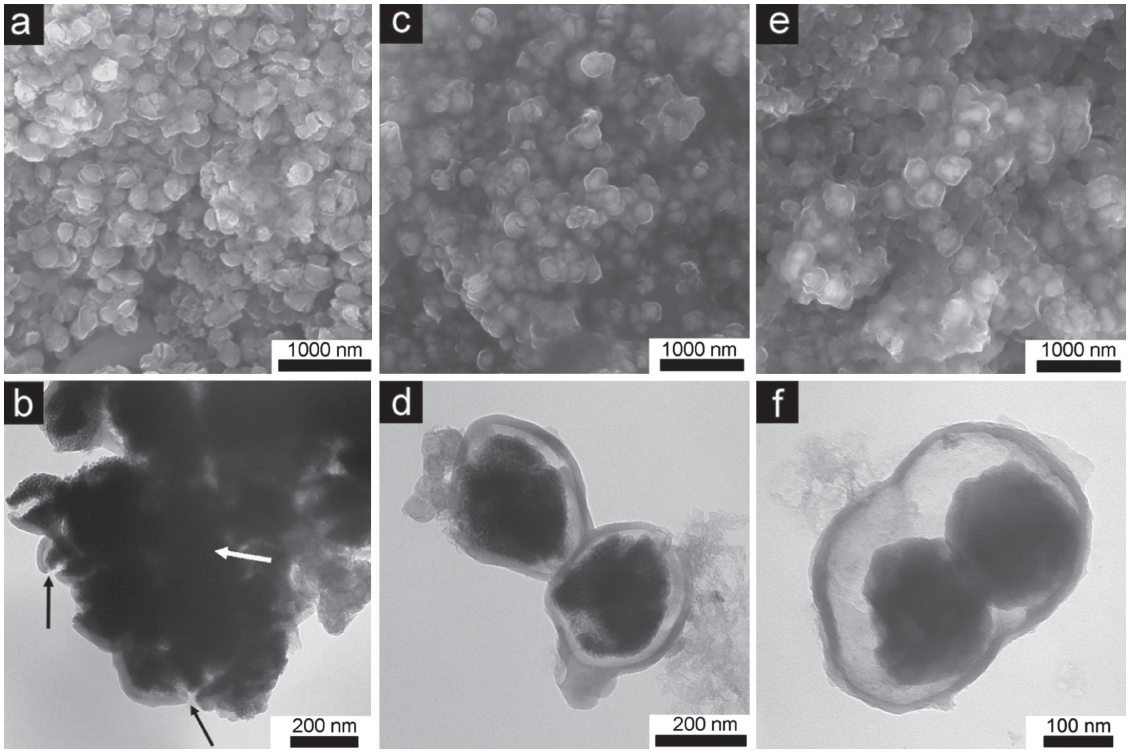

Figure 5. SEM and TEM images of a,b) FeO_x@C-1, c,d) FeO_x@C-2, and e,f) FeO_x@C-3 after 100 cycles at 0.2 C (in their lithiated state).

can be observed after cycling (Figure 5a,b), indicating that the void space is not sufficient to fully accommodate the volume expansion. The rupture of the carbon shells re-exposes the active material to electrolyte and causes serious aggregation of the active material (indicated by the white arrow in Figure 5b). Due to the extensive rupture of the carbon shells and aggregation of active materials, the rapid capacity decay of FeO_x@C-1 is not surprising. For FeO_x@C-2, the void space is rationally designed to be slightly larger than the desirable value; thus, the FeO_x core can expand/contract freely upon lithiation/de-lithiation without breaking the carbon shell. Even after 100 discharge-charge cycles, the yolk–shell structures can be well-maintained (Figure 5c,d). Upon full lithiation, the FeO_x core occupies most of the void space (Figure 5d), which maximizes the volumetric density. In addition, the intact carbon shell provides a fixed surface for the growth of a stable SEI film, preventing the continual rupturing and reformation of SEI.[25–27] Due to the improved structural and SEI stability, FeO_x@C-2 manifests excellent cycling stability. For FeO_x@C-3, the void space is engineered to be much larger than the desirable value. Thus, the volume expansion of the FeO_x core can be fully accommodated and the yolk–shell structure remains intact (Figure 5e,f). However, even in its fully lithiated state, a large void can still be observed at one side of the carbon shell (Figure 5f). As a result, the volumetric capacity of FeO_x@C-3 is much lower than that of FeO_x@C-2 (Supporting Information, Figure S10). The cycling performance of FeO_x@C-3 is not as good as expected probably due to the poor contact between the FeO_x core and the conductive carbon shell, which severely disrupts the efficient transport of electrons and lithium ions from/to the core.[27]

3. Conclusion

In summary, FeO_x@C yolk–shell structures have been rationally designed and successfully synthesized. The void space between the FeO_x core and carbon shell has been engineered to fit the volume expansion during lithiation. With an optimized void space, the sample FeO_x@C-2 exhibits high reversible capacity (≈810 mA h g^{-1}) and excellent cycling stability (97.4% capacity retention for 100 cycles). In addition to iron oxide, our concept of optimizing the void space for the accommodation of volume variation can also be applied to other high-capacity anode materials, such as other TMOs, Sn and Si, which suffer from large volume expansion during lithiation cycling.

4. Experimental Section

Synthesis of FeO_x@C: Uniform α-Fe_2O_3 nanocrystals were synthesized by the hydrothermal method. In a typical procedure, $FeCl_3$ (2 mmol) and L-arginine (0.5 mmol) were dissolved in distilled water (100 mL) to form a clear light yellow solution. Subsequently, the solution was transferred into a Teflon-lined stainless steel autoclave and kept at 150 °C for 12 hours. After cooling down to room temperature, the precipitate was collected by centrifugation, washed with deionized water, and dried at 50 °C. The α-Fe_2O_3@SiO_2 core-shell nanoparticles were prepared by coating a silica layer onto α-Fe_2O_3 nanoparticles through the hydrolysis and condensation of tetraethoxysilane (TEOS)

in a water-alcohol-ammonia solution.[36] Briefly, α-Fe_2O_3 (66.7 mg) nanoparticles were re-dispersed in a mixture of 2-propanol (160 mL) and distilled water (40 mL) by ultrasonication followed by the addition of $NH_3 \cdot H_2O$ (2 mL, 25–28 wt%). Afterwards, a given amount of TEOS (50, 150, and 400 µL) was added dropwise into the mixture under stirring. The mixture was then kept stirring for 4 hours at room temperature. The α-Fe_2O_3@SiO_2 core-shell nanoparticles were obtained after centrifugation, washing and drying. For carbon coating, the as-prepared α-Fe_2O_3@SiO_2 core-shell nanoparticles were dispersed in Tris-buffer (25 mL, 10 mM, pH = 8.5) by ultrasonication for 1 h. After that, dopamine hydrochloride (50 mg) was added and the mixture was kept stirring for 24 hours. In this process, the dopamine polymerized and coated the surface of the α-Fe_2O_3@SiO_2 nanoparticles.[37] The obtained α-Fe_2O_3@SiO_2@poly-dopamine nanoparticles were then annealed at 700 °C for 5 h under Ar to convert the poly-dopamine into carbon. After washing with 2 M NaOH for 12 h to remove the silica layer, FeO_x@C yolk–shell nanoparticles were obtained.

Materials Characterization: The morphology and structure of the samples were investigated by a field emission SEM (JEOL 7001F) operated at 15 kV and TEM, (Tecnai F20) at 200 kV. TGA was carried out on a METTLER TOLEDO TGA/DSC1 STAR^e System under air flow (25–800 °C, 5 °C min^{-1}). XRD patterns were collected on a Rigaku Miniflex X-ray Diffractometer with Co Kα radiation (λ = 0.179 nm). X-ray photoelectron spectra (XPS) were collected on a Kratos Axis ULTRA X-ray photoelectron spectrometer using a monochromatic Al KR (1486.6 eV) X-ray source and a 165 mm hemispherical electron energy analyzer.

Electrochemical Measurements: The electrochemical measurements were carried out on an MTI 8 Channel Battery Analyzer at room temperature. Lithium metal chips were used as both the counter electrode and reference electrode. The working electrode was prepared using active material, conductive acetylene black, and polyvinylidene fluoride (PVDF) binder in a weight ratio of 80:10:10. The electrolyte was composed of 1 M $LiPF_6$ in a mixture of ethylene carbonate, dimethyl carbonate, and diethyl carbonate (1:1:1 in volume). The electrode was punched into small disks with a diameter of 13 mm. Swagelok-type cells were fabricated in an Ar-filled glovebox with moisture and oxygen concentrations below 0.1 ppm. CV measurements were performed on a Solartron 1480 MultiStat instrument a scan rate of 0.1 mV s^{-1} between 0.001 V and 3.0 V.

Supporting Information

Supporting Information is available from the Wiley Online Library or from the author.

Acknowledgements

The authors acknowledge the Australian Research Council for financial support. The authors also acknowledge the facilities, the scientific and technical assistance from Centre for Microscopy and Microanalysis at the University of Queensland.

Received: January 18, 2014
Revised: February 19, 2014
Published online: April 1, 2014

[1] P. G. Bruce, S. A. Freunberger, L. J. Hardwick, J. M. Tarascon, *Nat. Mater.* **2012**, *11*, 19.
[2] J. M. Tarascon, M. Armand, *Nature* **2001**, *414*, 359.
[3] P. Poizot, S. Laruelle, S. Grugeon, L. Dupont, J. M. Tarascon, *Nature* **2000**, *407*, 496.
[4] L. Taberna, S. Mitra, P. Poizot, P. Simon, J. M. Tarascon, *Nat. Mater.* **2006**, *5*, 567.
[5] J. Jiang, Y. Y. Li, J. P. Liu, X. T. Huang, C. Z. Yuan, X. W. Lou, *Adv. Mater.* **2012**, *24*, 5166.
[6] W. M. Zhang, X. L. Wu, J. S. Hu, Y. G. Guo, L. J. Wan, *Adv. Funct. Mater.* **2008**, *18*, 3941.
[7] F. Han, D. Li, W. C. Li, C. Lei, Q. Sun, A. H. Lu, *Adv. Funct. Mater.* **2013**, *23*, 1692.
[8] Z. Y. Wang, L. Zhou, X. W. Lou, *Adv. Mater.* **2012**, *24*, 1903.
[9] X. Wang, X. L. Wu, Y. G. Guo, Y. T. Zhong, X. Q. Cao, Y. Ma, J. N. Yao, *Adv. Funct. Mater.* **2010**, *20*, 1680.
[10] Y. J. Hong, M. Y. Son, Y. C. Kang, *Adv. Mater.* **2013**, *25*, 2279.
[11] J. Y. Wang, N. L. Yang, H. J. Tang, Z. H. Dong, Q. Jin, M. Yang, D. Kisailus, H. J. Zhao, Z. Y. Tang, D. Wang, *Angew. Chem. Int. Ed.* **2013**, *52*, 6417.
[12] L. Zhou, H. Y. Xu, H. W. Zhang, J. Yang, S. B. Hartono, K. Qian, J. Zou, C. Z. Yu, *Chem. Commun.* **2013**, *49*, 8695.
[13] B. Wang, H. B. Wu, L. Zhang, X. W. Lou, *Angew. Chem. Int. Ed.* **2013**, *52*, 4165.
[14] B. Wang, J. S. Chen, H. B. Wu, Z. Y. Wang, X. W. Lou, *J. Am. Chem. Soc.* **2011**, *133*, 17146.
[15] C. Lei, F. Han, D. Li, W. C. Li, Q. Sun, X. Q. Zhang, A. H. Lu, *Nanoscale* **2013**, *5*, 1168.
[16] X. J. Zhu, Y. W. Zhu, S. Murali, M. D. Stollers, R. S. Ruoff, *ACS Nano* **2011**, *5*, 3333.
[17] G. M. Zhou, D. W. Wang, F. Li, L. L. Zhang, N. Li, Z. S. Wu, L. Wen, G. Q. Lu, H. M. Cheng, *Chem. Mater.* **2010**, *22*, 5306.
[18] H. W. Zhang, L. Zhou, C. Z. Yu, *RSC Adv.* **2014**, *4*, 495.
[19] N. Q. Zhao, S. Wu, C. N. He, Z. Y. Wang, C. S. Shi, E. Z. Liu, J. J. Li, *Carbon* **2013**, *57*, 130.
[20] S. Wu, Z. Y. Wang, C. N. He, N. Q. Zhao, C. S. Shi, E. Z. Liu, J. J. Li, *J. Mater. Chem. A* **2013**, *1*, 11011.
[21] X. W. Lou, C. M. Li, L. A. Archer, *Adv. Mater.* **2009**, *21*, 2536.
[22] J. M. Jeong, B. G. Choi, S. C. Lee, K. G. Lee, Y. B. L. Chang, H. U. Lee, S. Kwon, G. Lee, C. S. Lee, Y. S. Huh, *Adv. Mater.* **2013**, *25*, 6250.
[23] Y. Zhao, J. X. Li, C. X. Wu, Y. H. Ding, L. H. Guan, *ChemPlusChem* **2012**, *77*, 748.
[24] L. Zhan, Y. L. Wang, W. M. Qiao, L. C. Ling, S. B. Yang, *Electrochim. Acta* **2012**, *78*, 440.
[25] N. Liu, H. Wu, M. T. McDowell, Y. Yao, C. M. Wang, Y. Cui, *Nano Lett.* **2012**, *12*, 3315.
[26] H. Wu, G. Y. Zheng, N. A. Liu, T. J. Carney, Y. Yang, Y. Cui, *Nano Lett.* **2012**, *12*, 904.
[27] B. Wang, X. L. Li, X. F. Zhang, B. Luo, Y. B. Zhang, L. J. Zhi, *Adv. Mater.* **2013**, *25*, 3560.
[28] W. M. Zhang, J. S. Hu, Y. G. Guo, S. F. Zheng, L. S. Zhong, W. G. Song, L. J. Wan, *Adv. Mater.* **2008**, *20*, 1160.
[29] K. T. Lee, Y. S. Jung, S. M. Oh, *J. Am. Chem. Soc.* **2003**, *125*, 5652.
[30] Z. W. Seh, W. Y. Li, J. J. Cha, G. Y. Zheng, Y. Yang, M. T. McDowell, P. C. Hsu, Y. Cui, *Nat. Commun.* **2013**, *4*, 1131.
[31] W. D. Zhou, Y. C. Yu, H. Chen, F. J. DiSalvo, H. D. Abruna, *J. Am. Chem. Soc.* **2013**, *135*, 16736.
[32] C. N. He, S. Wu, N. Q. Zhao, C. S. Shi, E. Z. Liu, J. J. Li, *ACS Nano* **2013**, *7*, 4459.
[33] S. H. Lee, S.-H. Yu, J. E. Lee, A. Jin, D. J. Lee, N. Lee, H. Jo, K. Shin, T.-Y. Ahn, Y.-W. Kim, H. Choe, Y.-E. Sung, T. Hyeon, *Nano Lett.* **2013**, *13*, 4249.
[34] C. R. Jarvis, M. J. Lain, M. V. Yakovleva, Y. Gao, *J . Power Sources* **2006**, *162*, 800.
[35] W. Wei, S. Yang, H. Zhou, I. Lieberwirth, X. Feng, K. Müllen, *Adv. Mater.* **2013**, *25*, 2909.
[36] Y. Deng, D. Qi, C. Deng, X. Zhang, D. Zhao, *J. Am. Chem. Soc.* **2008**, *130*, 28.
[37] R. Liu, S. M. Mahurin, C. Li, R. R. Unocic, J. C. Idrobo, H. J. Gao, S. J. Pennycook, S. Dai, *Angew. Chem. Int. Ed.* **2011**, *50*, 6799.